AGU PUBLICATIONS

JGR

Journal of Geophysical Research: Space Physics

RESEARCH ARTICLE
10.1002/2016JA023646

Transition from global to local control of dayside reconnection from ionospheric-sourced mass loading

B. Zhang[1], O. J. Brambles[2], P. A. Cassak[3], J. E. Ouellette[4,5], M. Wiltberger[1], W. Lotko[1,2], and J. G. Lyon[4]

[1]High Altitude Observatory, National Center for Atmospheric Research, Boulder, Colorado, USA, [2]Thayer School of Engineering, Dartmouth College, Hanover, New Hampshire, USA, [3]Department of Physics and Astronomy, West Virginia University, Morgantown, West Virginia, USA, [4]Department of Physics and Astronomy, Dartmouth College, Hanover, New Hampshire, USA, [5]Department of Computer and Information Systems, Vermont Technical College, Randolph, Vermont, USA

Key Points:
- A transition from global control to local control on dayside reconnection occurs with dayside mass loading
- Magnetosheath response to changes in local reconnection rate depends on the amount of mass loading
- The control of dayside reconnection potential is determined by the role of enhanced magnetic pressure in the magnetosheath

Supporting Information:
- Supporting Information S1

Correspondence to:
B. Zhang,
binzheng@ucar.edu

Citation:
Zhang, B., O. J. Brambles, P. A. Cassak, J. E. Ouellette, M. Wiltberger, W. Lotko, and J. G. Lyon (2017), Transition from global to local control of dayside reconnection from ionospheric-sourced mass loading, *J. Geophys. Res. Space Physics*, *122*, 9474–9488, doi:10.1002/2016JA023646.

Received 1 NOV 2016
Accepted 12 JUL 2017
Accepted article online 17 JUL 2017
Published online 22 SEP 2017

©2017. American Geophysical Union. All Rights Reserved.

Abstract We have conducted a series of controlled numerical simulations to investigate the response of dayside reconnection to idealized, ionosphere-sourced mass loading processes to determine whether they affect the integrated dayside reconnection rate. Our simulation results show that the coupled solar wind-magnetosphere system may exhibit both local and global control behaviors depending on the amount of mass loading. With a small amount of mass loading, the changes in local reconnection rate affects magnetosheath properties only weakly and the geoeffective length in the upstream solar wind is essentially unchanged, resulting in the same integrated dayside reconnection rate. With a large amount of mass loading, however, the magnetosheath properties and the geoeffective length are significantly affected by slowing down the local reconnection rate, resulting in an increase of the magnetic pressure in the magnetosheath, with a significant reduction in the geoeffective length in the upstream solar wind and in the integrated dayside reconnection rate. In this controlled simulation setup, the behavior of dayside reconnection potential is determined by the role of the enhanced magnetic pressure in the magnetospheath due to magnetospheric mass loading. The reconnection potential starts to decrease significantly when the enhanced magnetic pressure alters the thickness of the magnetosheath.

1. Introduction

Magnetic reconnection at the Earth's dayside magnetopause is a key process in the interaction between the solar wind (SW) and the magnetosphere-ionosphere-thermosphere(M-I-T) system because it drives the circulation of magnetospheric plasmas and regulates the transport of electromagnetic energy. Thus, a clear understanding of what controls the integrated dayside reconnection rate is crucial to both space physics research and space weather forecasting.

The physical process that controls dayside reconnection is currently an area of considerable debate within the space physics community. The local control hypothesis suggests that the integrated dayside reconnection rate is controlled by the local plasma parameters on both magnetosheath and magnetosphere sides of the reconnection site [*Borovsky et al.*, 2008, 2013]. In this hypothesis, the local plasma parameters control the local reconnection rate along the dayside magnetopause with the sum representing the integrated reconnection rate, or the reconnection potential, as shown in Figure 1. In contrast, the global control hypothesis suggests that the integrated dayside reconnection rate is controlled by the forces acting on the flux tubes in the magnetosheath, which is primarily determined by the upstream solar wind parameters [*Lopez et al.*, 2010, 2016]. The two hypotheses are not necessarily inconsistent with each other since the local plasma parameters in the magnetosheath and magnetosphere depend upon the global transport pattern produced by the upstream solar wind conditions. Both hypotheses have been used in the development of coupling functions for predicting the energy input from the upstream SW to the M-I-T system. However, the two hypotheses diverge on predicting the response of the global reconnection rate when the local reconnection rate is significantly altered. The local reconnection rate depends on the mass densities and magnetic field strengths on the magnetospheric and magnetopause sides of the reconnection site [*Borovsky et al.*, 2008]. Magnetopause mass loading via terrestrial-sourced ions, including cold H^+ from the plasmasphere, cold O^+ from the ionosphere,

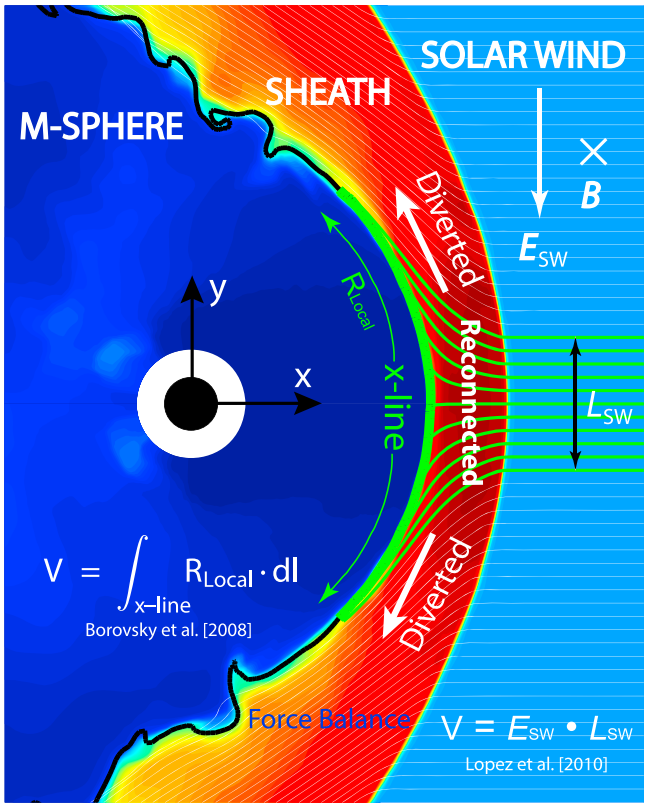

Figure 1. A schematic plot showing the local control and global control hypotheses of the integrated dayside magnetic reconnection rate *V*. E_{SW} is the solar wind electric field and L_{SW} is the geoeffective length in the solar wind.

and hot O^+ from the warm plasma cloak, is one of the physical processes that can change the local reconnection rate by altering the magnetospheric mass density.

Satellite observations have confirmed the existence of mass loading processes at the dayside magnetopause [e.g., *Spasojević et al.*, 2003; *Chandler and Moore*, 2003]. A statistical analysis using data acquired during Time History of Events and Macroscale Interactions during Substorms (THEMIS) spacecraft magnetopause crossings showed plasmaspheric plumes to be present at the dayside magnetopause during 12.5% of the crossings, with increasing in the mass density from 1 amu/cm^{-3} to 120 amu/cm^{-3} correlated with increasing in the polar cap index [*Walsh et al.*, 2013]. Event-based in situ measurements provided evidence that these plumes mass load the dayside magnetosphere and reduce the Alfvén speed on the magnetospheric side of the magnetopause resulting in a decrease in the local reconnection rate [*Walsh et al.*, 2014a, 2014b]. Recent observations on the dynamic throat aurora also suggest magnetospheric cold plasma flowing into the magnetopause reconnection site on the dayside [*Han et al.*, 2016].

During enhanced geomagnetic activity, ionospheric O^+ ions become an important source of magnetospheric plasma, which impacts the dynamics associated with the coupling between the SW and M-I-T system [e.g., *Chappell et al.*, 1987; *Nosé et al.*, 2003; *Engwall et al.*, 2009; *Kitamura et al.*, 2010; *Denton et al.*, 2014; *Kronberg et al.*, 2014; *Chappell*, 2015; *Haaland et al.*, 2015; *Welling et al.*, 2015b; *Wiltberger*, 2015]. For example, *Borovsky* [2013] showed that ions originating from the warm plasma cloak might contribute greater mass density (up to 100 amu/cm^{-3}) and have a greater impact on the dayside reconnection rate than plasmaspheric ions during storm time events. Recent analysis based on the Cluster satellites suggested that hot magnetospheric O^+ ions, along with the hot magnetospheric H^+ ions participate in the dayside reconnection process [*Wang et al.*, 2015a]. Further analysis of the Cluster satellite data showed that the magnetospheric O^+ ions can contribute up to 30% of the mass density at the magnetopause, which should inevitably reduce the local reconnection rate for such events [*Wang et al.*, 2015b; *Lee et al.*, 2015]. Based on these observational studies, questions remain on how terrestrial-sourced mass loading impacts dayside SW-M interactions, especially regarding control of dayside reconnection [e.g., *Fuselier et al.*, 2016], and whether the local or global control hypothesis provides a more accurate description of dayside reconnection when mass loading occurs.

With magnetopause mass loading, the local control hypothesis predicts a decrease in the integrated dayside reconnection rate due to the local modifications of reconnection rate, while the global control hypothesis predicts no changes in the integrated dayside reconnection rate since the forces in the magnetosheath are not affected by local reconnection. To understand the incompatibility between the two hypotheses, *Zhang et al.* [2016a] used controlled global simulations with idealized mass loading to show that the coupled SW-M-I system may exhibit both local control and global control behaviors depending on the mass density of ionospheric-sourced mass loading at the dayside magnetopause. With a small amount of mass loading, the SW-M system exhibits global control behavior of the dayside reconnection potential by spatially redistributing

the dayside reconnection rate so that the integrated reconnection rate remains unchanged [*Lopez*, 2016]. The spatially redistribution of reconnection rates has also been seen in the magnetotail with ionospheric O^+ mass loading [*Garcia et al.*, 2010; *Wiltberger et al.*, 2010; *Zhang et al.*, 2016b] and at the dayside magnetopause with mass loading by plasmaspheric H^+ plumes [*Borovsky et al.*, 2008; *Ouellette et al.*, 2016]. With a large amount of mass loading, the SW-M system exhibits local control behavior of the dayside reconnection potential through the significant decrease of the local reconnection rate at the magnetopause. A decrease in reconnection potential and ionospheric potential has also been seen in previous global simulations with ionospheric-sourced mass loading [e.g., *Winglee et al.*, 2002; *Glocer et al.*, 2009a, 2009b; *Brambles et al.*, 2010, 2013; *Welling and Zaharia*, 2012; *Yu and Ridley*, 2013a; *Ouellette et al.*, 2013].

The controlled mass loading simulation results in *Zhang et al.* [2016a] showed a transition regime between global control and local control mechanisms, depending on the mass density of magnetopause mass loading. According to *Zhang et al.* [2016a], when the ionospheric mass loading is less than 8 amu/cm^{-3} at the dayside magnetopause for the solar wind conditions in the simulations, the dayside reconnection potential remains unchanged, which is in the global control regime. When the ionospheric-sourced mass density is greater than 32 amu/cm^{-3}, the dayside reconnection potential decreases approximately linearly with the mass density, which is in the local control regime. In this particular case with idealized ionospheric outflow, the mass density range between 8 and 32 amu/cm^{-3} may be regarded as the transition regime. Note that the observed density range of mass loading at the magnetopause is within the simulated density range for both global control and local control of the dayside reconnection.

In this paper, we focus on the physical origin of the transition regime associated with the control of dayside reconnection reported by *Zhang et al.* [2016a]. The controlled global simulations presented in *Zhang et al.* [2016a] are further analyzed in order to investigate the response of the magnetosheath properties due to magnetospheric mass loading. The paper is organized as follows. Section 2 describes details of the numerical simulation setup and the physical considerations associated with the design of the controlled simulation. Section 3 describes the response of magnetosheath properties due to dayside mass loading and the physical origins of the reconfiguration of the magnetosheath and the control of dayside reconnection. Section 4 summarizes the results.

2. Simulation Information

Previous global simulations have shown that when ionospheric outflow is introduced, the coupled SW-M-I system may be reconfigured through direct or indirect pathways. Direct mass loading is not the only process leading to changes in the dayside reconnection potential. Figure 2 shows several possible pathways in which ionospheric outflow can influence dayside reconnection. It is clear that using an empirical or physics-based outflow model in this study may influence the dayside reconnection in variety of ways. For example, the causally regulated, empirical O^+ ion outflow model developed by *Brambles et al.* [2011] introduces dynamic outflow distributions and fluxes in the dayside cusp region and nightside auroral latitudes. These outflowing ions populate different regions of the magnetosphere, which introduce a variety of feedback effects in the coupling between the solar wind, magnetosphere, and ionosphere [e.g., *Brambles et al.*, 2010; *Welling et al.*, 2011; *Welling and Zaharia*, 2012; *Yu and Ridley*, 2013a, 2013b; *Moore et al.*, 2014; *Welling et al.*, 2015a; *Welling and Liemohn*, 2016; *Varney et al.*, 2016b]. Therefore, it is very difficult to use empirical or physics-based outflow models to design controlled numerical experiments to study the direct effects of mass loading without changing the whole SW-M-I dynamics.

To isolate the effect of dayside mass loading on the reconnection rate, we designed a set of numerical experiments using the multifluid version of the Lyon-Fedder-Mobarry global magnetosphere model (MFLFM) [*Lyon et al.*, 2004] so that the influences from the red pathways shown in Figure 2 are minimized to the fullest extent possible. The detailed simulation setups and SW/IMF (interplanetary magnetic field) driving conditions are described in *Zhang et al.* [2016a]. Here we repeat some of the key setups in order to help the readers understand the methodology and interpret the simulation results in the following sections. In the finite-volume solver, ionospheric outflow ions are introduced as surface fluxes (mass flux, momentum flux, and energy flux) at the low-altitude computational cell faces (2 R_E geocentric) between 58° and 68° magnetic latitude, 1930–2130 magnetic local time (MLT) on the dusk side, and 0230–0430 MLT on the dawn side. The spatial distribution of parallel outflow number flux mapped to ionospheric altitude (100 km) is shown in Figure 3a.

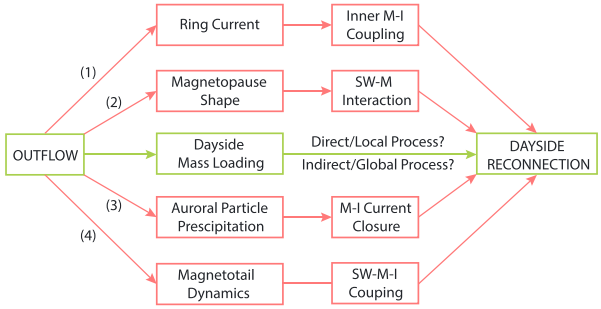

(1): Glocer et al. [2009a]; Moore et al. [2014]; Welling et al. [2011, 2015]
(2): Brambles et al. [2010]; Welling et al., [2012]
(3): Brambles et al. [2010];
(4): Wiltberger et al. [2010]; Garcia et al., [2016]; Zhang et al. [2016b]

Figure 2. Possible pathways of impacting dayside reconnection via causally driven, empirical ionospheric outflow. The green pathway is the one that is studied in this paper.

Based on the outflow location setup, eight runs with different ion atomic mass (M_i = 0, 2, 4, 8, 16, 32, 64, and 128 amu) are performed, while the parallel number flux ($n_i v_{i\|}$), the parallel kinetic energy flux ($M_i n_i v_{i\|}^2 v_{i\|}$), and the parallel thermal energy flux ($M_i n_i c_{si}^2 v_{i\|}$) introduced at the low-altitude boundary surface are kept the same:

$$\int_{r=2\,R_E} n_i \mathbf{v}_{i\|} \cdot d\mathbf{S} = \text{const} \quad (1)$$

$$\int_{r=2\,R_E} M_i n_i v_{i\|}^2 \bar{\mathbf{v}}_{i\|} \cdot d\mathbf{S} = \text{const} \quad (2)$$

$$\int_{r=2\,R_E} M_i n_i c_{si}^2 \bar{\mathbf{v}}_{i\|} \cdot d\mathbf{S} = \text{const.} \quad (3)$$

Therefore, the surface-integrated outflow number flux, parallel momentum flux, and thermal energy flux rate introduced in the system remain the same in each controlled simulation. Note that the M_i = 0 case is just a single-fluid simulation with no outflow, which is used as the baseline simulation The detailed implementation and tests of the above outflow boundary conditions are described in *Varney et al.* [2016a]. In order to remove dawn-dusk asymmetries, the corotation is switched off in the controlled simulations. For the oxygen outflow run (M_{O^+} = 16), the outflow number density n_{O^+} is set to be 10^2 cm^{-3}, the parallel velocity $v_{O^+\|}$ is set to be 40 km/s, and the sound speed c_{sO^+} is set to be 20 km/s, which gives a parallel number flux of 4×10^8 cm^{-2} s^{-1} and an integrated hemispheric outflow rate of 0.8×10^{26} s^{-1}. The integrated outflow rate used in the set of controlled simulations is within the statistical estimations of observed outflow rates for moderate driving conditions [e.g., *Cully et al.*, 2003]. When the outflow atomic mass changes, the outflow number density n_i scales as $n_{O^+}\sqrt{M_i/M_{O^+}}$, the parallel velocity $v_{i\|}$ scales as $v_{O^+\|}\sqrt{M_{O^+}/M_i}$, and the sound speed c_{si} scales as $c_{sO^+}\sqrt{M_{O^+}/M_i}$ to satisfy equations (1)–(3). Although the thermal energy flux introduced in each simulation remains the same, the plasma pressure of the outflow population in the inner magnetosphere scales as a function of $\sqrt{M_i}$. However, the variation in the bulk plasma temperature in the inner magnetosphere is less than 10%, suggesting that the outflow plasma is not significantly heated in the plasma sheet. Note that the purpose of using nonphysical ionospheric ion atomic mass is to investigate the effects of different magnetospheric mass on dayside reconnection rather than to represent realistic ionospheric outflow populations. With this idealized low-altitude outflow flux specification, the spatial extent of the simulated mass loading region at the dayside magnetopause is illustrated schematically in Figure 3b. The multifluid version of the Lyon-Fedder-Mobarry (LFM) code uses nonorthogonal stretched spherical grid to simulate the magnetosphere, with resolution emphasized near the magnetopause, the bow shock and in the inner magnetosphere. In the controlled simulations, the grid resolution along the radial direction near the dayside magnetopause is approximately 0.135 R_E.

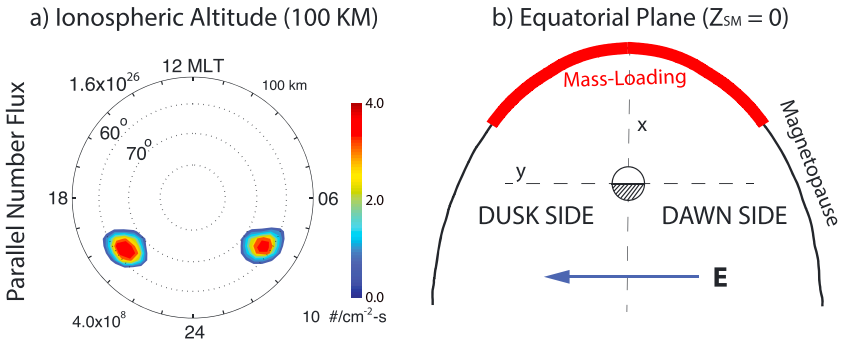

Figure 3. (a) The average distribution of parallel outflow number density mapped to ionospheric altitude (100 km). (b) The region of mass loading at the equatorial magnetopause.

To simplify the analysis, each controlled simulation is driven by the same, idealized solar wind (SW) and interplanetary magnetic field (IMF) conditions. In each simulation, after the magnetosphere was preconditioned (without outflow) for 4 h (IMF $B_z = -5$ nT between 00:00 and 02:00 and $B_z = +5$ nT between 02:00 and 04:00 simulation time, ST), IMF B_z was then set to be southward with a magnitude of 5 nT for 12 h (04:00–16:00 ST) to enable dayside magnetic reconnection in the equatorial plane since the magnetosphere is mostly closed when driven by northward IMF. The IMF B_x and B_y components were set to zero and the SW $V_x = 400$ km/s, $V_y = V_z = 0$. The adiabatic SW fluid has a number density of 5 cm^{-3} and a sound speed of 40 km/s, respectively. The dipole tilt was set to zero in order to remove hemispheric asymmetries, and the ionospheric Pedersen conductance was set to be spatially uniform at 5 mhos in order to remove possible dawn-dusk asymmetries in the magnetospheric reconnection caused by ionospheric electrodynamics [*Zhang et al.*, 2012; *Lotko et al.*, 2014] and also to minimize pathway (3) shown in Figure 2. The ionospheric outflow is switched on at 6:00 ST when the system is in a steady magnetosphere convection (SMC) state. Note that since the outflow is introduced on closed magnetic field lines during the SMC state, the total pressure in the inner magnetosphere is not significantly affected by adding outflow, so pathway (1) is also minimized.

In the LFM simulation, magnetic reconnection is enabled through numerical resistivity; thus, reconnection in the code is predominantly averaging error; opposing magnetic flux enters a single cell and is averaged out of existence [*Lyon et al.*, 2004]. The rate of reconnection is determined only by the conditions external to the actual reconnection region through the conservation of mass, momentum, and magnetic flux. Outside the reconnection region, the numerical method of the MHD solver is accurate enough to make sure that numerical reconnection does not occur, regardless of the size of the computational grid. Therefore, in cases where the external flow toward the reconnection site is zero, the reconnection rate is effectively also zero. When reconnection is forced by convergent flow, the reconnection rate in the simulation is constrained by a Petschek-like inflow condition to be a fraction (≈0.1) of the Alfven speed in the inflow. *Ouellette et al.* [2013] have shown that the normalized reconnection rate in the LFM simulation is insensitive to the grid resolution on the nightside. We have performed numerical experiments with different grid resolutions and found similar reconnection rates (≈0.1) on the dayside when driven by southward IMF (see supporting information S1).

3. Results and Discussion

Figure 4 shows the distributions of equatorial outflow number density averaged between 12:00 and 16:00 ST in the seven controlled simulations. In each simulation, the distribution of average outflow number density in the reconnection inflow region of the equatorial magnetosphere peaks around 1400 MLT with number density near 1 cm^{-3}. The minimum outflow number density occurs near the noon sector due to the "Earth shadow" effect—the magnetospheric convection toward the noon sector is so slow that little outflow plasma is transported to the x axis. For the $M_i = 1$ case, the mass density at the dayside magnetopause is near the lower limit of the statistical mass loading from plasmaspheric plumes observed by the THEMIS satellite, while for the $M_i = 128$ case, the mass density of the simulated mass loading at the dayside magnetopause is approximately the upper limit of the statistical mass density observed by the THEMIS satellites [*Walsh et al.*, 2013]. Note that the dynamic mass loading process in the simulation is different from the averaged density distributions shown in Figure 4, which are calculated using 4 h averaged states; therefore, the mass loading region seems to have large magnetic local time (MLT) extensions peaks between 13 and 15 MLT in the afternoon sector and 9–11 MLT in the morning sector. In the dynamic simulation, the instantaneous distributions of outflow plumes advecting from the nightside have approximately spatial extension of 1.5 h MLT with varying density and locations on the dayside. The background plasma population in the controlled simulation is H^+ with solar wind origin. The average number density of the H^+ plasma near the dayside magnetopause is approximately 0.1 cm^{-3} in the baseline simulation, which decreases to 0.031 cm^{-3} as M_i increases to 128.

Figure 5a shows the temporal response of average outflow number density in three controlled simulations with $M_i = 0$ (baseline), $M_i = 4$ (a small amount of mass loading), and $M_i = 128$ (a large amount of mass loading). The average outflow number density is calculated from the region between 14 and 15 MLT in the equatorial magnetosphere that is 0.5 R_E away from the magnetopause. In the controlled simulations, the low-altitude ionospheric outflow patches are switched on at 06:00 ST, indicated by the black dashed lines in Figure 5. As shown in Figure 5a, the ionospheric outflow number density near the dayside magnetopause increases from 0 to 1 ions per cubic centimeter in approximately 3 h and remains about 1 cm^{-3} in the rest of the simulation time. The temporal response of the ionospheric outflow density near the magnetopause suggests that the mass loading process at the magnetopause enters a quasi-steady state after 09:00 ST.

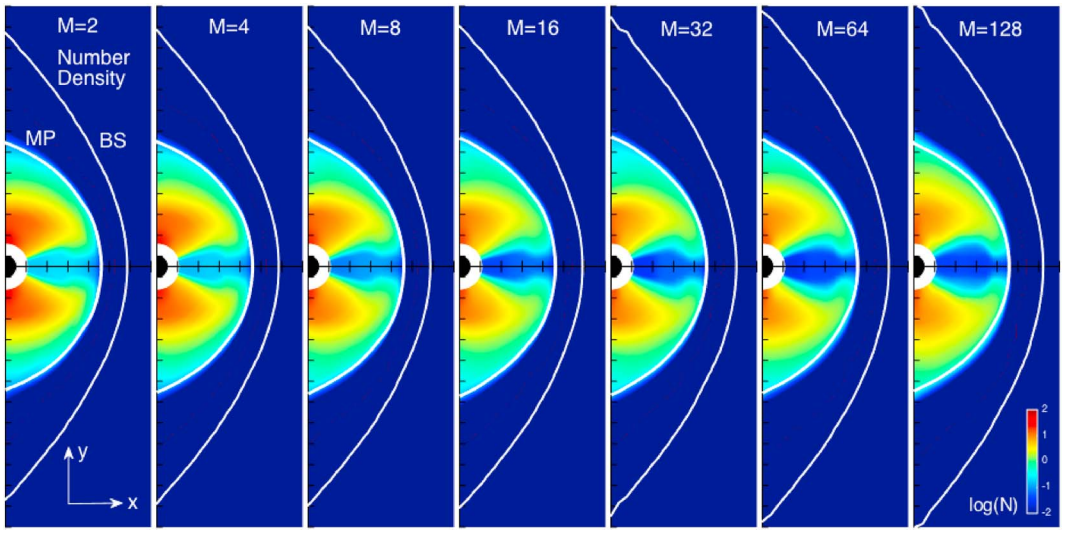

Figure 4. Average number density of the mass loading at the dayside magnetopause derived from the seven controlled simulations with different ion mass.

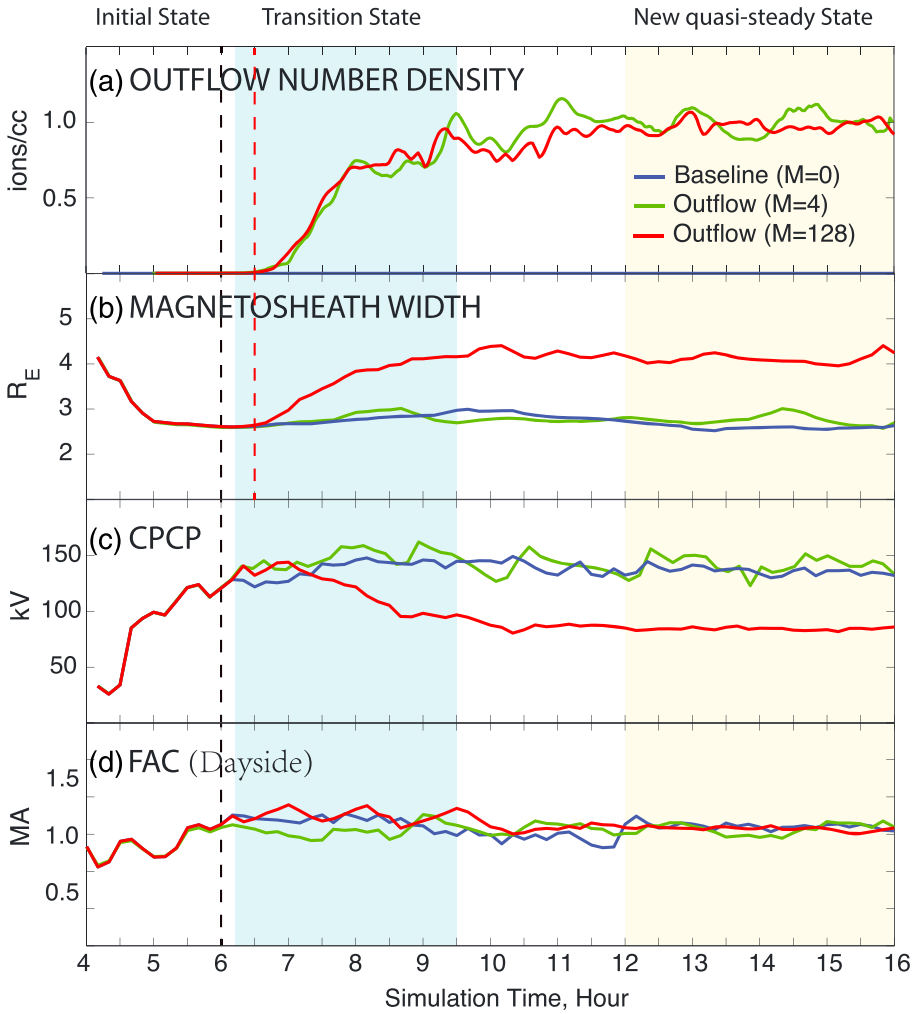

Figure 5. The dynamics responses of (a) outflow number density at the magnetopause inflow region, (b) the width of the magnetosheath along the *x* axis, (c) the cross polar cap potential, and (d) the integrated field-aligned current flowing into the dayside ionosphere. The blue curves are from the baseline simulation without outflow ($M_i = 0$); the green and red curves are derived from the run with $M_i = 4$ and $M_i = 128$, respectively.

Figure 5b shows the corresponding changes in the thickness of the magnetosheath along the x axis (i.e., the distance between the magnetopause and bow shock along the x axis) derived from the three simulations with $M_i = 0$, 4, and 128, respectively. In the $M_i = 4$ run, the thickness of magnetosheath does not change significantly with mass loading. However, in the $M_i = 128$ run, the thickness of magnetosheath increases from 2.8 R_E to 4.1 R_E over a time of approximately 3 h, which correlates well with the density increase at the dayside magnetopause as shown in Figure 5a. The correlation between of the magnetosheath thickness and outflow number density in the $M_i = 128$ case suggests that the magnetosheath responses instantaneously to the dayside mass loading process.

Figure 5c shows the response of cross-polar cap potential (CPCP) in the three controlled simulations. Compared to the baseline case with $M_i = 0$, the CPCP in the $M_i = 4$ case does not show a significant change in the overall magnitude after 10:00 ST. In the $M_i = 128$ case, a 60 kV drop in CPCP occurs after 10:00 ST. The reduction in CPCP is consistent with the decrease of dayside reconnection potential (≈70 kV), which is a consequence of reducing local reconnection rate at the dayside magnetopause. Figure 5d shows the temporal variations of the integrated dayside field-aligned current (FAC) from the three controlled simulations. The fact that there are only small changes in the integrated dayside FAC is consistent with the fact that the shape of the dayside magnetopause (shown in Figure 4) and the currents flowing at the dayside magnetopause are not significantly influenced by the idealized mass loading process. Therefore, pathway (2) shown in Figure 2 is minimized in the controlled simulations (and the change in magnetosheath width does not originate from the change in the shape of magnetopause). According to the temporal variations shown in Figure 5, the system evolves from the initial state (04:00–06:00 ST) to a new quasi-steady state (10:00–16:00 ST) through a transition state (07:00–10:00 ST). The next results are calculated from the new quasi-steady state between 12:00 and 16:00 ST.

Figures 6a–6c show the shape of the magnetopause, the bow shock, the geoeffective length (L_{eff}) in the equatorial plane, together with the distribution of magnetic pressure ($B^2/2\mu_0$) in the equatorial plane calculated from the three simulations with $M_i = 0$, $M_i = 4$, and $M_i = 128$, respectively. For visualizing the magnetosheath, the much higher magnetic pressure earthward of the magnetopause is set to be uniformly 0.1 nPa so that the color plots are not dominated by the large, saturated values inside the magnetopause. The geoeffective length is approximated by tracing average upstream solar wind velocity streamlines originated from the equatorial plane that intersect the magnetopause merging line [*Lopez et al.*, 2010], as bounded by the yellow streamlines shown in Figures 6a–6c. The streamlines are traced using a fourth-order Runge-Kutta method. Note that the calculation of the exact value of the geoeffective length is difficult due to the dynamic variations of the magnetopause boundary in the simulation. Thus, the corresponding average geoeffective length determined by the streamline tracing method using average plasma flow vectors is just an estimation with uncertainties. In the streamline tracing process, together with the intersection criterion for defining the geoeffective length, the z location of the streamlines at $x = 0$ is also used to determine whether the boundary of the geoeffective length is appropriately determined. If we use the criterion that the z location of the streamline at $x = 0$ must be greater than 1.0 R_E (at least two grid cells above the equatorial plane), the uncertainty of the upstream geoeffective length is approximately 0.55 R_E on each side of the x axis. Therefore, the error associated with the definition of the geoeffective length could be around 1.1 R_E.

Compared to the baseline simulation, the geoeffective length in the $M_i = 4$ case remains approximately 10 R_E, suggesting that the dayside reconnection is in the global control regime. In the simulation with $M_i = 128$, the geoeffective length decreases by approximately 5 R_E compared to the baseline simulation (corresponding to a 60 kV potential reduction), suggesting that the dayside reconnection is in the local control regime. This potential decrease calculated using the reduction in the geoeffective length is consistent with the change in the dayside reconnection potential as shown in *Zhang et al.* [2016a]. The 5 R_E reduction is greater than the uncertainty in the calculation of the geoeffective length, suggesting that the decrease in the estimated geoeffective length is very unlikely a pure numerical effect, although the actual value of the reduction might be not accurate. The decrease of the geoeffective length in the $M_i = 128$ case suggests that not only the local reconnection rates are reduced by the mass loading process, properties of magnetosheath are also modified such that more solar wind flux tubes are diverted in the magnetosheath. The comparison between the two mass loading simulations leads to two key questions: (1) why is the magnetosheath width changed in the $M_i = 128$ case but not the $M_i = 4$ case and (2) what caused the decrease in the geoeffective length in the $M_i = 128$ case?

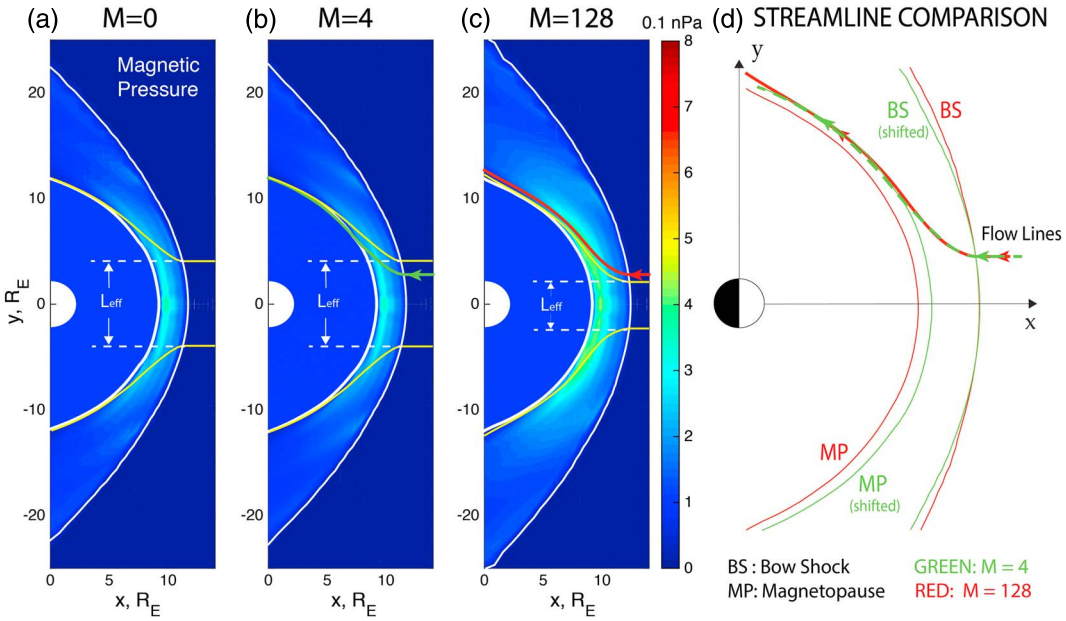

Figure 6. Magnetic pressure in the equatorial plane calculated from (a) baseline, (b) a small amount of mass loading, and (c) a large amount of mass loading simulations. The geoeffective length is shown using yellow lines. (d) Comparisons between the two flow streamlines originated from the same location shown in Figures 6b and 6c.

The changes of magnetic pressure in the magnetosheath is the answer to explain the different behaviors of the system response in the two controlled simulations. Compared to the baseline case in Figure 6a, the average magnetic pressure in the magnetosheath in the $M_i = 4$ case does not change significantly as shown in Figure 6b. However, in the $M_i = 128$ case, the magnetic pressure in the magnetosheath increases approximately 30% compared to the baseline case, especially in the region near the magnetopause X line, suggesting magnetic flux piling-up occurs in the magnetosheath. A simple calculation can provide a first estimate of the increase in magnetic pressure. Define the initial state i as before the ionospheric outflow has reached the magnetopause and the final state f as after it has reached and a new steady state has been achieved. The total momentum flux must be the same in the solar wind, magnetosheath, and the magnetosphere side of the magnetopause. Since the solar wind momentum flux is unchanged, the magnetosheath momentum flux is unchanged. Then, evaluating the momentum flux just upstream of the magnetosheath edge of the magnetopause, we have

$$\frac{B_{s,i}^2}{2\mu_0} + n_{s,i}T_{s,i} + \rho_{s,i}v_{\mathrm{in},s,i}^2 = \frac{B_{s,f}^2}{2\mu_0} + n_{s,f}T_{s,f} + \rho_{s,f}v_{\mathrm{in},s,f}^2, \tag{4}$$

where the s subscript denotes the magnetosheath side of the magnetopause and v_{in} is the $-x$ directed magnetosheath flow, which at the magnetopause must equal the reconnection inflow speed (since we are considering the steady state). For simplicity, we assume that there is no compression of the magnetosheath that results from the increased magnetospheric mass, so that $n_{s,i}T_{s,i} = n_{s,f}T_{s,f}$. This may be a reasonable assumption for small ionospheric mass contributions but is not likely true for large ionospheric mass contributions. Note that equation (4) would not apply to an arbitrary crossing of the magnetopause and three-dimensional effects are important. However, if the cut through the magnetopause is taken radially outward at the subsolar point, then by the symmetric simulation setups, there would be no momentum transfer tangent to the magnetopause and the 2-D assumption is valid in equation (4).

For the inflow speed, it has been shown that the 2-D asymmetric reconnection theory [*Cassak and Shay*, 2007] quantitatively describes the local reconnection rate at the dayside magnetopause in the global geometry for due southward IMF and no dipole tilt [*Borovsky et al.*, 2008; *Ouellette et al.*, 2010; *Komar and Cassak*, 2016]. So we use $v_{\mathrm{in},s} = E/B_s$, with

$$E = \frac{B_s B_m}{B_s + B_m} v_{\mathrm{out}} \frac{2\delta}{L}, \tag{5}$$

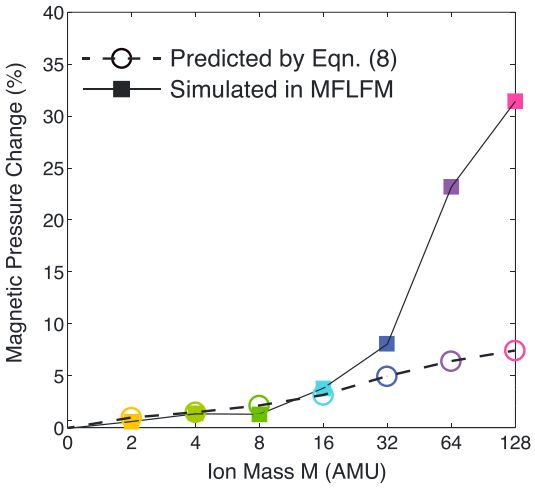

Figure 7. The comparison between the simulated percentage enhancement of average magnetic pressure in the magnetosheath and the corresponding percentage enhancement predicted by equation (8). The average magnetic pressure values are calculated in the magnetosheath between 09 and 15 MLT, and the inflow parameters used in equation (8) are calculated at 0.5 R_E away from the dayside X line.

where δ/L is the aspect ratio of the diffusion region, assumed to be 0.1 for fast reconnection (even in the asymmetric case) [*Cassak and Shay*, 2008; *Malakit et al.*, 2010], the m subscript denotes the values measured just on the magnetospheric side of the magnetosheath, and the asymmetric outflow speed is

$$v_{\text{out}}^2 = \frac{B_s B_m}{\mu_0} \frac{B_s + B_m}{\rho_s B_m + \rho_m B_s}. \tag{6}$$

Equations (5) and (6) of the present study are direct copies of equations (19) and (13) from *Cassak and Shay* [2007]. The inflow speeds differ in the initial i and final f states because ρ_m changes. Combining $v_{\text{in},s} = E/B_s$ with equations (5) and (6), we obtain

$$v_{\text{in},s} = 0.2 \frac{B_m}{B_s + B_m} \left[(B_s B_m/\mu_0)(B_s + B_m)/(\rho_s B_m + \rho_m B_s) \right]^{1/2}. \tag{7}$$

Substituting these into equation (4) and simplifying gives

$$\Delta\left(\frac{B_s^2}{2\mu_0}\right) = \frac{B_{s,i}^2}{2\mu_0} \frac{8B_{m,i}^2}{B_{s,i}(B_{s,i} + B_{m,i})} \left(\frac{\delta}{L}\right)^2 \left[1 - \frac{B_{m,f}^2}{B_{m,i}^2} \frac{B_{s,f}}{B_{s,i}} \frac{B_{s,i} + B_{m,i}}{B_{s,f} + B_{m,f}} \left(\frac{\rho_{s,f} B_{m,f}}{\rho_{s,f} B_{m,f} + \rho_{m,f} B_{s,f}}\right)\right], \tag{8}$$

where $\Delta(B_s^2/2\mu_0) = (B_{s,f}^2/2\mu_0) - (B_{s,i}^2/2\mu_0)$. This provides an estimate for the amount of magnetic flux pileup on the magnetosheath side of the magnetopause. Each of the quantities can readily be measured in the simulations. The comparison between the magnetic pressure enhancement predicted by equation (8), and the corresponding magnetic pressure enhancement derived from the three-dimensional simulation is shown in Figure 7. The percentage change of the average magnetic pressure in the magnetosheath is calculated at inflow regions 0.5 R_E away from the magnetopause within an MLT range between 0900 and 1500 MLT. The parameters for equation (8) are also calculated from 0.5 R_E away from the magnetopause. When $M_i \leq 16$, the simulated enhancement of magnetic pressure in the magnetosheath matches the prediction from the two-dimensional theory reasonably well. However, when $M_i \geq 32$, the simulated magnetic pressure enhancement in the magnetosheath is greater than a factor of 2 compared to the predictions from the two-dimensional theory. Note that the actual differences between the simulation and the 2-D theory prediction are sensitive to the choice of the location where the parameters are calculated, but significant divergence occurs when $M_i \geq 32$. It is possibly due to the fact that the 2-D calculation does not take the magnetosheath dynamics into account. It is also possible that the 2-D simplification in deriving equation (8) does not work well outside the local noon sector. Further investigations are needed to determine the physical origin of this difference.

As a consequence of enhanced magnetic pressure in the magnetosheath, the width of the magnetosheath in the $M_i = 128$ run is approximately 1.3 R_E wider than that in the $M_i = 4$ run. Figure 6d shows the comparison

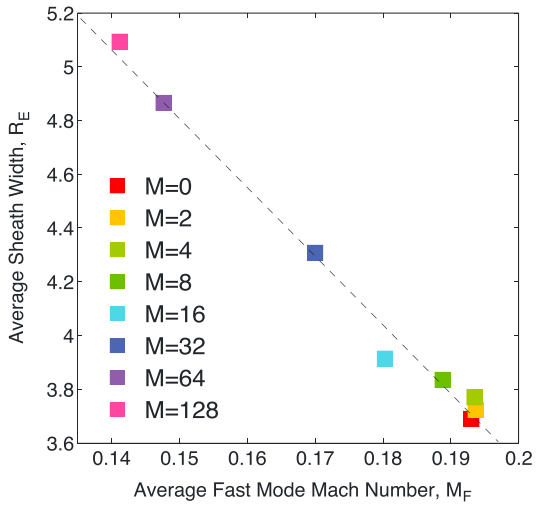

Figure 8. The relationship between the average fast mode Mach number in the magnetosheath and the average width of the magnetosheath.

of two plasma flow lines derived from the $M_i = 4$ run and the $M_i = 128$ run. The streamline in each case originates from the same location in the equatorial plane ($x = 12\,R_E$, $y = 4\,R_E$, and $z = 0\,R_E$). In order to make direct comparisons, the bow shock and magnetopause in the $M_i = 4$ run are shifted by 1.3 R_E toward the Sun so that the two bow shocks are aligned at the x axis. This artificial shift is only for diagnostic purposes such that the two plasma flow lines in the two controlled simulations turn at the same x location; that is, the curvature of the flow lines can be directly compared. Note that the radius of curvature of the equatorial plasma flow line depends on the total perpendicular force acting on the solar wind flux tube. As shown in Figure 6d, the curvature of the two flow lines from the two controlled simulations are approximately identical, suggesting that the perpendicular force diverting solar wind flux tubes in the magnetosheath remains unchanged. We have also calculated the ∇p and the $J \times B$ terms in the magnetosheath (not shown) using the MHD output to confirm that (1) the average force in the magnetosheath is dominated by the pressure gradient term ∇p and (2) the ∇p terms in the $M_i = 4$ and the $M_i = 128$ run are approximately the same, especially near the locations where the curvature radius of the streamlines are minimum. The calculation of average force terms in the magnetosheath is consistent with the streamline behaviors shown in Figure 6d. The fact that the average force in the magnetosheath remains unchanged is mainly a consequence of the plasma in the magnetosheath being high beta since it is driven by high Alfvén Mach number solar wind conditions ($\bar{\beta}_{M_i=4} = 3.8$ and $\bar{\beta}_{M_i=128} = 3.0$), in which the forces are determined by fluid stresses rather than changes in magnetic stresses [*Lopez et al.*, 2010]. Therefore, given the fact that the forces are approximately the same, a thicker magnetosheath in the $M_i = 128$ case diverts more solar wind flux, resulting in a shorter geoeffective length as shown in Figure 6c and lower dayside reconnection potential.

The increase in magnetosheath width is a consequence of the decrease in the fast-mode Mach number M_F in the magnetosheath [*Chapman and Cairns*, 2003] which follows the magnetic pressure enhancement. Figure 8 shows the average M_F in the magnetosheath calculated between 09 and 15 MLT in the eight test simulations with increasing M_i. For $M_i \leq 8$, the change in M_F is relatively small (<5%), while $M_i \geq 16$, the average fast-mode Mach number drops from 0.192 to 0.141. Since the width of the magnetosheath is controlled by the fast-mode Mach number M_F, which determines the distance of magnetosonic waves traveling

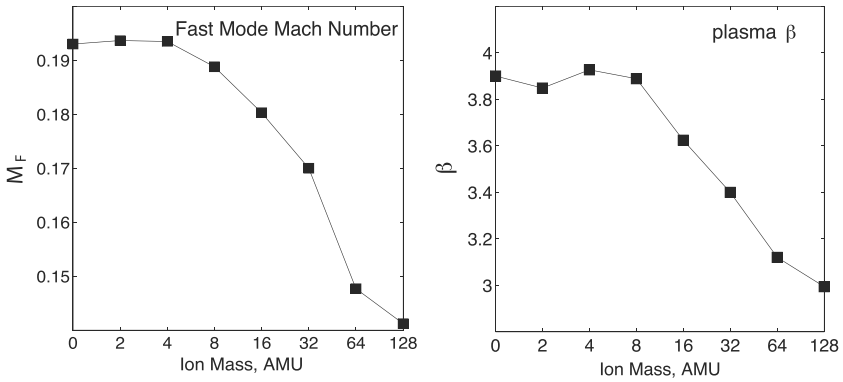

Figure 9. The average fast-mode Mach number and plasma beta in the sheath as a function of mass loading, calculated between 0900 and 1500 MLT in the magnetosheath.

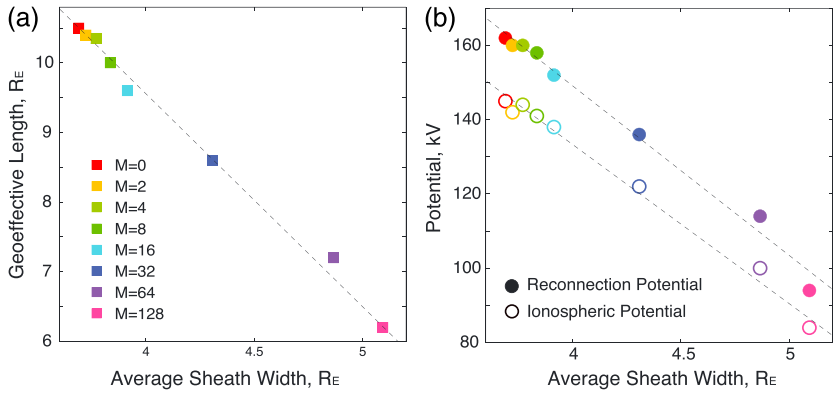

Figure 10. The relationship between the geoeffective length, dayside reconnection potential, and ionospheric potential versus the width of the magnetosheath.

from the magnetopause to the bow shock, with the same steady SW/IMF driving conditions in the controlled simulations, the width of magnetosheath increases from 3.7 R_E to 5.1 R_E as M_F decreases from 0.192 to 0.141. The relationships between the dayside mass loading and the simulated average M_F and plasma β in the magnetosheath calculated between 09 and 15 MLT are shown in Figure 9. As M_i increases from 0 to 8 amu, the average plasma β remains approximately 3.9. When M_i increases from 8 to 120 amu, the average plasma β decreases from 3.9 to 3.0. The transition point occurs near $M_i = 8$. In the controlled simulations, the changes in the simulated plasma β in the magnetosheath mainly occur near the magnetopause rather than the bow shock, which is consistent with the fact that the force balance near the bow shock is not significantly affected by the mass loading process at the dayside magnetopause as indicated by the curvature of the streamlines near the bow shock shown in Figure 6d.

Figure 10 shows the simulated geoeffective length, dayside reconnection potential, and ionospheric potential as functions of the average width of the magnetosheath. As shown in Figure 10a, the geoeffective length calculated in the upstream solar wind decreases approximately linearly with the increasing width of magnetosheath, which is qualitatively consistent with the flow-diverting scenario suggested by *Lopez et al.* [2010]. As a consequence, both the dayside reconnection potential (integrated along the magnetopause between 06 and 18 MLT) and ionospheric potential exhibit similar linear relationships with the average width of the magnetosheath as shown in Figure 10b. Although the transition behavior shown in Figure 9 is not very evident in Figure 10a, the difference in the simulations with $M_i \leq 8$ is less than 0.2 R_E, which is below the uncertainty level of the geoeffective length calculation. A similar transition behavior is also evident in the average magnitude of the magnetic field in the magnetosheath (not shown). This transition behavior is consistent with the response of the dayside reconnection potential shown in Figure 3 of *Zhang et al.* [2016a]. The difference between the reconnection potential and ionospheric potential is due to a loss of numerical accuracy in mapping equalpotentials along magnetic field lines because the magnetic field lines converge faster at low altitudes than the MFLFM's spherical grid. From the global control point of view, the relationship between the width of magnetosheath and the dayside reconnection potential suggests that when ionospheric-sourced mass loading occurs at the dayside magnetopause, local control of dayside reconnection potential is achieved when magnetic flux pileup in the flow stagnation region alters the magnetosheath properties and diminishes the transport of solar wind flux tubes to the magnetopause X line.

The controlled simulation set with ionospheric-sourced mass loading along the flanks of the dayside magnetopause exhibit changes in dayside reconnection that are predicted by both the global control and local control hypotheses. While $M_i = 4$ case changes the local reconnection rate (not shown, see Figure 2 of *Zhang et al.* [2016a] for the detailed distribution of the local reconnection rate), the ionospheric mass has a small effect on magnetosheath properties and little impact on the dayside reconnection potential. Alternatively, the reduction in local reconnection rates in the $M_i = 128$ simulation significantly impacts the magnetosheath properties that control solar wind-magnetosphere merging and the dayside reconnection potential. The comparison between the two cases suggests a possible physical origin of the transition from global control to local control of dayside reconnection. In the $M_i = 4$ case, when magnetic pressure enhancements (flux pileup) occurs in the magnetosheath due to magnetopause mass loading, the lifetime of the enhanced magnetic

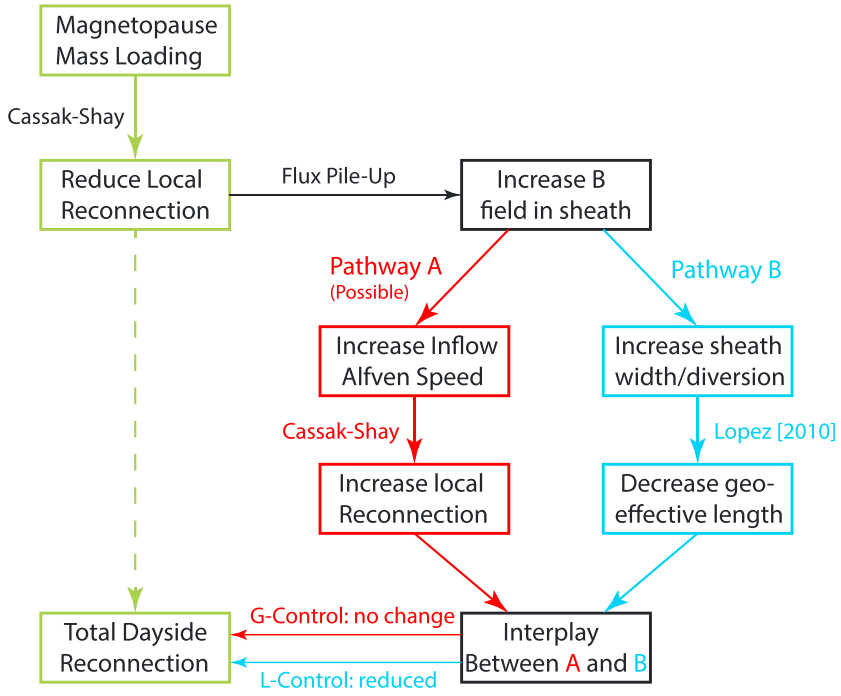

Figure 11. The pathways of modifying the integrated dayside reconnection rate via magnetopause mass loading.

pressure"blobs" in the magnetosheath is less than 2 min, which is much faster than the corresponding speed of the magnetosheath flows. While in the $M_i = 128$ case, the lifetime of the corresponding enhanced magnetic pressure blobs is around 10 min, which also move toward the flank regions with the same speed as the magnetosheath flow, suggesting the piled-up fluxes are diverted along the magnetopause. Therefore, the transition is mediated by the behavior of the enhanced magnetic pressure in the magnetosheath (Figure 11). Here we give one possible pathway that may explain the behavior of the enhanced magnetic pressure in the $M_i = 4$ case. The Cassak-Shay theory for two-dimensional asymmetric reconnection theory predicts an increase in the local reconnection rate when the magnetic pressure in the magnetosheath is enhanced due to flux pileup. The increase in the local reconnection rate may not be in exactly the same location as the pileup magnetic flux due to the dynamic evolution of the magnetosheath. This increase compensates for an otherwise reduced reconnection rate due to mass loading in the magnetospheric inflow region, resulting in little change in the dayside reconnection potential (pathway A in Figure 11). On the other hand, the three-dimensional simulations show that the enhanced magnetic pressure may alter the upstream conditions via increasing the width of the magnetosheath so that less solar wind flux is reconnected at the magnetopause, resulting in a significant reduction in the geoeffective length and dayside reconnection potential, which is the *Lopez et al.* [2010] model (pathway B in Figure 11). This pathway is consistent with the interpretation discussed in *Birn and Hesse* [2007]; that is, the change in reconnection rate may be caused by changing the local plasma parameters at the inflow region due to magnetic flux pileup. Therefore, when mass loading occurs at the dayside magnetopause, the control of dayside reconnection is determined by the dominant process associated with the enhanced magnetic pressure in the magnetosheath. Note that further analysis is needed to quantify both the possible physical process associated with pathway A and the parameters controlling the pathway B. As shown in the idealized simulations, the mass density of ionosphere-sourced mass loading is clearly one of the factors regulating the transition. Other factors may include the spatial extension and the temporal variation of the source of mass loading. Ionospheric conductance may also play an important role. Note that in the physical processes shown in Figure 11, the pathways indicated in red as shown in Figure 2 are ignored in this set of controlled simulations, which means that in the real SW-M-I system, the control of dayside reconnection potential may be much more complicated than the idealized simulation results discussed in this study.

The simulation results based on multifluid global magnetospheric simulations suggest a possible way of quantifying the transition regime between the two hypotheses via examining the role of the enhanced magnetic pressure in the magnetosheath due to different mass loading specifications. Thus, the response

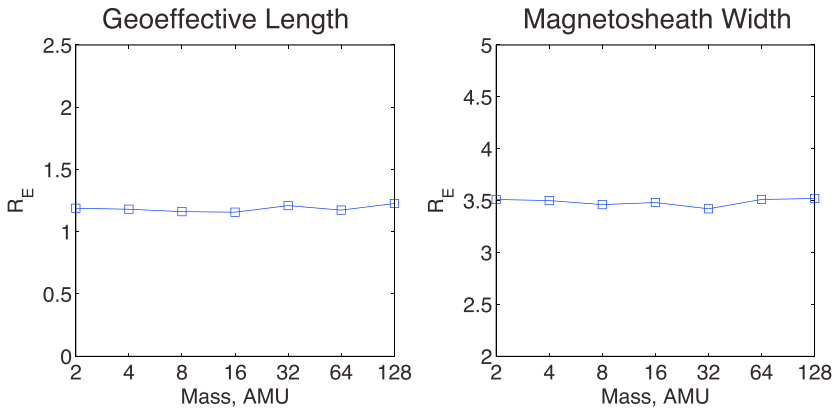

Figure 12. The response of the geoeffective length and the width of the magnetosheath along the *x* axis using the same set of ionospheric sourced mass loading enabled at the low-altitude boundary, driven by pure northward IMF conditions (B_z = +5 nT). The SW conditions are chosen to be the same as the southward IMF simulations.

of the magnetosheath properties due to mass loading is the key to resolve the discrepancies between the two hypotheses. The question remains on how the real magnetosphere responds to localized mass loading at the dayside magnetopause. Note that the simulated responses of the magnetosheath width and the geoeffective length are only valid for southward IMF conditions. When the magnetosphere is closed, both the width of the magnetosheath and the geoeffective length in the solar wind do not change with increasing amount of nightside, ionospheric sourced mass loading. Figure 12 shows the response of the geoeffective length and the width of the magnetosheath along the *x* axis using the same set of ionospheric sourced mass loading enabled at the low-altitude boundary, driven by pure northward IMF conditions (B_z = +5 nT) with SW conditions remain the same as the southward IMF simulations. Although the outflow rates might not be physical for northward IMF driving conditions, it is clear that the geoeffective length is approximately 1.17 R_E and the width of the magnetosheath is approximately 3.5 R_E regardless of the amount of mass loading. It is also important to note that further numerical simulations with more physics modules included are necessary in order to investigate the response of the magnetosheath and dayside reconnection [e.g., *Welling and Zaharia*, 2012]. Further observational studies from multiple satellite measurements at the dayside magnetopause are also needed to quantify the response of Earth's magnetosheath due to dayside mass loading under dynamic upstream driving conditions.

4. Conclusions

In this study, we investigate the physical origin of the transition from global control to local control on dayside reconnection potential using idealized, controlled mass loading simulations based on multifluid global simulations. The controlled simulations are designed to minimize the effects of magnetopause inflation, outflow-enhanced inner magnetosphere pressure/ring current, and ionospheric conductance on the dayside reconnection. The idealized mass loading simulations show that when local reconnection rates are reduced via ionospheric-sourced ions, the magnetic pressure in the magnetosheath increases due to flux pileup. In this particular simulation setup, the dayside reconnection transition regime depends upon the role of the enhanced magnetic pressure in the magnetosheath. With idealized mass loading, when the mass density at the dayside magnetopause inflow region is less than 8 amu/cm^{-3}, the enhanced magnetic pressure in the magnetosheath inflow region is less than 3% and compensates the reduced location reconnection rate such that the integrated reconnection rate remains unchanged. When the mass density at the dayside magnetopause inflow region is greater than 16 amu/cm^{-3}, the enhanced magnetic pressure in the magnetosheath inflow region causes a significant reconfiguration of the magnetosheath by increasing the width of the sheath. As a consequence, the geoeffective length decreases due to the fact that more solar wind flux is diverted by a thicker magnetosheath, resulting in a significant decrease in the integrated dayside reconnection rate. The agreement between the simulated local reconnection rates and the theoretical predictions based on the Cassak-Shay equation on the dayside improves as M_i increases from 0 to 128 in the controlled simulations, which is also seen in the controlled plasmaspheric simulation results analyzed in *Ouellette et al.* [2016].

From the global control point of view, the local control hypothesis is a system-level reconfiguration when a large amount of mass loading occurs at the dayside magnetopause; that is, the local control of dayside reconnection potential is achieved by altering the magnetosheath properties through reducing local reconnection rates such that less solar wind flux tubes are transported to the magnetopause X line. From the local control point of view, the dayside solar wind-magnetosphere merging is not entirely determined by the upstream solar wind parameters. Ionospheric-source mass loading may reduce the geoeffective length in the upstream solar wind via modifying local reconnection rate. Other factors such as the ionospheric conductivities may also play an important role.

Acknowledgments
The research was supported by the projects NSFAGS-1404599, National Aeronautics and Space Administration grants NNX16AF75G and NNX16AG76G. Computing resources were provided by the CISL at the National Center for Atmospheric Research (NCAR) under project UDRT0006. NCAR is sponsored by the National Science Foundation. Simulation data are available from B. Zhang (binzheng@ucar.edu).

References

Borovsky, J. E. (2013), Physical improvements to the solar wind reconnection control function for the Earth's magnetosphere, *J. Geophys. Res. Space Physics*, *118*, 2113–2121, doi:10.1002/jgra.50110.

Borovsky, J. E., M. Hesse, J. Birn, and M. M. Kuznetsova (2008), What determines the reconnection rate at the dayside magnetosphere?, *J. Geophys. Res.*, *113*, A07210, doi:10.1029/2007JA012645.

Brambles, O. J., W. Lotko, P. A. Damiano, B. Zhang, M. Wiltberger, and J. Lyon (2010), Effects of causally driven cusp O^+ outflow on the storm time magnetosphere-ionosphere system using a multifluid global simulation, *J. Geophys. Res.*, *115*, A00J04, doi:10.1029/2010JA015469.

Brambles, O. J., W. Lotko, B. Zhang, M. Wiltberger, J. Lyon, and R. J. Strangeway (2011), Magnetosphere sawtooth oscillations induced by ionospheric outflow, *Science*, *332*(6034), 1183–1186, doi:10.1126/science.1202869.

Brambles, O. J., W. Lotko, B. Zhang, J. Ouellette, J. Lyon, and M. Wiltberger (2013), The effects of ionospheric outflow on ICME and SIR driven sawtooth events, *J. Geophys. Res. Space Physics*, *118*, 6026–6041, doi:10.1002/jgra.50522.

Birn, J., and M. Hesse (2007), Reconnection rates in driven magnetic reconnection, *Phys. Plasmas*, *14*(3), 082306, doi:10.1063/1.2.752510.

Cassak, P. A., and M. A. Shay (2007), Scaling of asymmetric magnetic reconnection: General theory and collisional simulations, *Phys. Plasmas*, *14*, 102–114, doi:10.1063/1.2795630.

Cassak, P. A., and M. A. Shay (2008), Scaling of asymmetric Hall magnetic reconnection, *Geophys. Res. Lett.*, *35*, L19102, doi:10.1029/2008GL035268.

Chandler, M. O., and T. E. Moore (2003), Observations of the geopause at the equatorial magnetopause: Density and temperature, *Geophys. Res. Lett.*, *30*(16), 1869, doi:10.1029/2003GL017611.

Chapman, J. F., and I. H. Cairns (2003), Three-dimensional modeling of Earth's bow shock: Shock shape as a function of Alfvén Mach number, *J. Geophys. Res.*, *108*(A5), 1174, doi:10.1029/2002JA009569.

Chappell, C. R. (2015), The role of the ionosphere in providing plasma to the terrestrial magnetosphere—An historical overview, *Space Sci. Rev.*, *192*(1–4), 5–25, doi:10.1007/s11214-015-0168-5.

Chappell, C. R., T. E. Moore, and J. H. Waite Jr. (1987), The ionosphere as a fully adequate source of plasma for the Earth's magnetosphere, *J. Geophys. Res.*, *92*(A6), 5896–5910, doi:10.1029/JA092iA06p05896.

Cully, C. M., E. F. Donovan, A. W. Yau, and G. G. Arkos (2003), Akebono/Suprathermal Mass Spectrometer observations of low-energy ion outflow: Dependence on magnetic activity and solar wind conditions, *J. Geophys. Res.*, *108*(A2), 1093, doi:10.1029/2001JA009200.

Denton, R. E., K. Takahashi, M. F. Thomsen, J. E. Borovsky, H. J. Singer, Y. Wang, J. Goldstein, P. C. Brandt, and B. W. Reinisch (2014), Evolution of mass density and O^+ concentration at geostationary orbit during storm and quiet events, *J. Geophys. Res. Space Physics*, *119*, 6417–6431, doi:10.1002/2014JA019888.

Engwall, E., A. I. Eriksson, C. M. Cully, M. André, P. A. Puhl-Quinn, H. Vaith, and R. Torbert (2009), Survey of cold ionospheric outflows in the magnetotail, *Ann. Geophys.*, *27*(8), 3185–3201, doi:10.5194/angeo-27-3185-2009.

Fuselier, S. A., et al. (2016), Magnetospheric ion influence on magnetic reconnection at the duskside magnetopause, *Geophys. Res. Lett.*, *43*, 1435–1442, doi:10.1002/2015GL067358.

Garcia, K. S., V. G. Merkin, and W. J. Hughes (2010), Effects of nightside O^+ outflow on magnetospheric dynamics: Results of multifluid MHD modeling, *J. Geophys. Res.*, *115*, A00J09, doi:10.1029/2010JA015730.

Glocer, A., G. Toth, T. Gombosi, and D. Welling (2009a), Modeling ionospheric outflows and their impact on the magnetosphere, initial results, *J. Geophys. Res.*, *114*, A05216, doi:10.1029/2009JA014053.

Glocer, A., G. Toth, Y. J. Ma, T. Gombosi, J.-C. Zhang, and L. M. Kistler (2009b), Multifluid block-adaptive-tree solar wind roe-type upwind scheme: Magnetospheric composition and dynamics during geomagnetic storms-Initial results, *J. Geophys. Res.*, *114*, A12203, doi:10.1029/2009JA014418.

Haaland, S., et al. (2015), Estimation of cold plasma outflow during geomagnetic storms, *J. Geophys. Res. Space Physics*, *120*, 10,622–10,639, doi:10.1002/2015JA021810.

Han, D.-S., Y. Nishimura, L. R. Lyons, H.-Q. Hu, and H.-G. Yang (2016), Throat aurora: The ionospheric signature of magnetosheath particles penetrating into the magnetosphere, *Geophys. Res. Lett.*, *43*, 1819–1827, doi:10.1002/2016GL068181.

Kitamura, N., et al. (2010), Observations of very-low-energy (<10 eV) ion outflows dominated by O^+ ions in the region of enhanced electron density in the polar cap magnetosphere during geomagnetic storms, *J. Geophys. Res.*, *115*, A00J06, doi:10.1029/2010JA015601.

Komar, C. M., and P. A. Cassak (2016), The local dayside reconnection rate for oblique interplanetary magnetic fields, *J. Geophys. Res. Space Physics*, *121*, 5105–5120, doi:10.1002/2016JA022530.

Kronberg, E. A., et al. (2014), Circulation of heavy ions and their dynamical effects in the magnetosphere: Recent observations and models, *Space Sci. Rev.*, *184*, 173–235, doi:10.1007/s11214-014-0104-0.

Lee, S. H., H. Zhang, Q.-G. Zong, Y. Wang, A. Otto, Rème H., and K.-H. Glassmeier (2015), Asymmetric ionospheric outflow observed at the dayside magnetopause, *J. Geophys. Res. Space Physics*, *120*, 3564–3573, doi:10.1002/2014JA020943.

Lopez, R. E. (2016), The integrated dayside merging rate is controlled primarily by the solar wind, *J. Geophys. Res. Space Physics*, *121*, 4435–4445, doi:10.1002/2016JA022556.

Lopez, R. E., R. Bruntz, E. J. Mitchell, M. Wiltberger, J. G. Lyon, and V. G. Merkin (2010), Role of magnetosheath force balance in regulating the dayside reconnection potential, *J. Geophys. Res.*, *115*, A12216, doi:10.1029/2009JA014597.

Lotko, W., R. H. Smith, B. Zhang, J. E. Ouellette, O. J. Brambles, and J. G. Lyon (2014), Ionospheric control of magnetotail reconnection, *Science*, *345*(6193), 184–187, doi:10.1126/science.1252907.

Lyon, J., J. Fedder, and C. Mobarry (2004), The Lyon-Fedder-Mobarry (LFM) global MHD magnetospheric simulation code, *J. Atmos. Sol. Terr. Phys.*, *66*(15–16), 1333–1350, doi:10.1016/j.jastp.2004.03.020.

Malakit, K., M. A. Shay, P. A. Cassak, and C. Bard (2010), Scaling of asymmetric magnetic reconnection: Kinetic particle-in-cell simulations, *J. Geophys. Res.*, *115*, A10223, doi:10.1029/2010JA015452.

Moore, T. E., M.-C. Fok, and K. Garcia-Sage (2014), The ionospheric outflow feedback loop, *J. Atmos. Sol. Terr. Phys.*, *115–116*, 59–66, doi:10.1016/j.jastp.2014.02.002.

Nosé, M., R. W. McEntire, and S. P. Christon (2003), Change of the plasma sheet ion composition during magnetic storm development observed by the Geotail spacecraft, *J. Geophys. Res.*, *108*(A5), 1201, doi:10.1029/2002JA009660.

Ouellette, J., B. Rogers, M. Wiltberger, and J. Lyon (2010), Magnetic reconnection at the dayside magnetopause in global Lyon-Fedder-Mobarry simulations, *J. Geophys. Res.*, *115*, A08222, doi:10.1029/2009JA014886.

Ouellette, J. E., O. J. Brambles, J. G. Lyon, W. Lotko, and B. N. Rogers (2013), Properties of outflow-driven sawtooth substorms, *J. Geophys. Res. Space Physics*, *118*, 3223–3232, doi:10.1002/jgra.50309.

Ouellette, J. E., J. G. Lyon, O. J. Brambles, B. Zhang, and W. Lotko (2016), The effects of plasmaspheric plumes on dayside reconnection, *J. Geophys. Res. Space Physics*, *121*, 4111–4118, doi:10.1002/2016JA022597.

Spasojević, M., J. Goldstein, D. L. Carpenter, U. S. Inan, B. R. Sandel, M. B. Moldwin, and B. W. Reinisch (2003), Global response of the plasmasphere to a geomagnetic disturbance, *J. Geophys. Res.*, *108*(A9), 1340, doi:10.1029/2003JA009987.

Varney, R. H., M. Wiltberger, B. Zhang, W. Lotko, and J. G. Lyon (2016a), Influence of ion outflow in coupled geospace simulations: 1. Physics-based ion outflow model development and sensitivity study, *J. Geophys. Res. Space Physics*, *121*, 9671–9687, doi:10.1002/2016JA022777.

Varney, R. H., M. Wiltberger, B. Zhang, W. Lotko, and J. G. Lyon (2016b), Influence of ion outflow in coupled geospace simulations: 2. Sawtooth oscillations driven by physics-based ion outflow, *J. Geophys. Res. Space Physics*, *121*, 9688–9700, doi:10.1002/2016JA022778.

Walsh, B. M., D. G. Sibeck, Y. Nishimura, and V. Angelopoulos (2013), Statistical analysis of the plasmaspheric plume at the magnetopause, *J. Geophys. Res. Space Physics*, *118*, 4844–4851, doi:10.1002/jgra.50458.

Walsh, B. M., J. C. Foster, P. J. Erickson, and D. G. Sibeck (2014a), Simultaneous ground- and space-based observations of the plasmaspheric plume and reconnection, *Science*, *343*(6175), 1122–1125, doi:10.1126/science.1247212.

Walsh, B. M., T. D. Phan, D. G. Sibeck, and V. M. Souza (2014b), The plasmaspheric plume and magnetopause reconnection, *Geophys. Res. Lett.*, *41*, 223–228, doi:10.1002/2013GL058802.

Wang, S., L. M. Kistler, C. G. Mouikis, Y. Liu, and K. J. Genestreti (2015a), Hot magnetospheric O^+ and cold ion behavior in magnetopause reconnection: Cluster observations, *J. Geophys. Res. Space Physics*, *119*, 9601–9623, doi:10.1002/2014JA020402.

Wang, S., L. M. Kistler, C. G. Mouikis, and S. M. Petrinec (2015b), Dependence of the dayside magnetopause reconnection rate on local conditions, *J. Geophys. Res. Space Physics*, *120*, 6386–6408, doi:10.1002/2015JA021524.

Welling, D. T., and M. W. Liemohn (2016), The ionospheric source of magnetospheric plasma is not a black box input for global models, *J. Geophys. Res. Space Physics*, *121*, 5559–5565, doi:10.1002/2016JA022646.

Welling, D. T., and S. G. Zaharia (2012), Ionospheric outflow and cross polar cap potential: What is the role of magnetospheric inflation?, *Geophys. Res. Lett.*, *39*, L23101, doi:10.1029/2012GL054228.

Welling, D. T., V. K. Jordanova, S. G. Zaharia, A. Glocer, and G. Toth (2011), The effects of dynamic ionospheric outflow on the ring current, *J. Geophys. Res.*, *116*, A00J19, doi:10.1029/2010JA015642.

Welling, D. T., V. K. Jordanova, A. Glocer, G. Toth, M. W. Liemohn, and D. R. Weimer (2015a), The two-way relationship between ionospheric outflow and the ring current, *J. Geophys. Res. Space Physics*, *120*, 4338–4353, doi:10.1002/2015JA021231.

Welling, D. T., M. André, I. Dandouras, D. Delcourt, A. Fazakerley, D. Fontaine, and A. Yau (2015b), The Earth: Plasma sources, losses, and transport processes, *Space Sci. Rev.*, *192*(1–4), 145–208, doi:10.1007/s11214-015-0187-2.

Wiltberger, M. (2015), Review of global simulation studies of effect of ionospheric outflow on magnetosphere-ionosphere system dynamics, in *Magnetotails in the Solar System*, edited by A. Keiling, C. M. Jackman, and P. A. Delamere, pp. 373–392, John Wiley, Hoboken, N. J., doi:10.1002/978111884232.

Wiltberger, M., W. Lotko, J. G. Lyon, P. Damiano, and V. Merkin (2010), Influence of cusp O^+ outflow on magnetotail dynamics in a multifluid MHD model of the magnetosphere, *J. Geophys. Res.*, *115*, A00J05, doi:10.1029/2010JA015579.

Winglee, R. M., D. Chua, M. Brittnacher, G. K. Parks, and G. Lu (2002), Global impact of ionospheric outflows on the dynamics of the magnetosphere and cross-polar cap potential, *J. Geophys. Res.*, *107*(A9), 1237, doi:10.1029/2001JA000214.

Yu, Y., and A. J. Ridley (2013a), Exploring the influence of ionospheric O^+ outflow on magnetospheric dynamics: Dependence on the source location, *J. Geophys. Res. Space Physics*, *118*, 1711–1722, doi:10.1029/2012JA018411.

Yu, Y., and A. J. Ridley (2013b), Exploring the influence of ionospheric O^+ outflow on magnetospheric dynamics: The effect of outflow intensity, *J. Geophys. Res. Space Physics*, *118*, 5522–5531, doi:10.1002/jgra.50528.

Zhang, B., W. Lotko, O. Brambles, P. Damiano, M. Wiltberger, and J. Lyon (2012), Magnetotail origins of auroral Alfvénic power, *J. Geophys. Res.*, *117*, A09205, doi:10.1029/2012JA017680.

Zhang, B., O. J. Brambles, W. Lotko, J. E. Ouellette, and J. G. Lyon (2016a), How does mass loading impact local versus global control on dayside reconnection?, *Geophys. Res. Lett.*, *43*, 1837–1844, doi:10.1002/2016GL068005.

Zhang, B., O. J. Brambles, W. Lotko, J. E. Ouellette, and J. G. Lyon (2016b), Role of ionopsheric O^+ ions on the generation of earthward plasmoids, *J. Geophys. Res Space Physics*, *120*, 1425–1435, doi:10.1002/2015JA021667.